

Quantum Communication Over Atmospheric Channels— A Framework for Optimizing Wavelength and Filtering

R. Nicholas Lanning,¹ Mark A. Harris,² Denis W. Oesch,² Michael D. Oliker,² and Mark T. Gruneisen¹

¹*Air Force Research Lab, Starfire Optical Range, Kirtland AFB, New Mexico 87116, USA**

²*Leidos, Albuquerque NM, United States*

(Dated: March 4, 2022)

Despite quantum networking concepts, designs, and hardware becoming increasingly mature, there is no consensus on the optimal wavelength for free-space systems. We present an in-depth analysis of a daytime free-space quantum channel as a function of wavelength and atmospheric spatial coherence (Fried coherence length). We choose quantum key distribution bit yield as a performance metric in order to reveal the ideal wavelength choice for an actual qubit-based protocol under realistic atmospheric conditions. Furthermore, our analysis represents a rigorous framework to analyze requirements for spatial, spectral, and temporal filtering. These results will help guide the development of free-space quantum communication and networking systems. In particular, our results suggest that shorter wavelengths should be considered for free-space quantum communication systems. Our results are also interpreted in the context of atmospheric compensation by higher-order adaptive optics.

PACS numbers: 03.67.Dd, 03.67.Hk, 42.50.Nn, 42.68.Bz, 42.79.Sz, 95.75.Qr

I. INTRODUCTION

Quantum networking concepts, designs, and hardware are becoming increasingly mature and in many ways transitioning to an engineering phase. Unlike fiber networks which suffer an exponential attenuation with propagation distance, free-space networks only suffer a quadratic loss due to geometric aperture-to-aperture coupling when approximated by the Friis equation [1, 2]. In principle, free-space quantum networks can enable global-scale quantum communication via satellite based nodes and quantum ground transceivers. This could facilitate distributed quantum computation, blind quantum computation, quantum-assisted imaging, and precise timing, to name just a few proposed applications [3–5]. An enduring problem is the ideal wavelength for free-space quantum communication over atmospheric channels, particularly in daytime conditions where filtering sky-noise photons is a formidable challenge [6–19].

Figure 1(a) illustrates the concept of spatially filtering optical noise at the field stop of an optical receiver. A primary optic of diameter D_R defines the entrance pupil and is followed by a field stop situated in the focal plane, a collimating lens, and a spectral filter. The field stop defines the solid-angle Field of View (FOV) and limits the number of sky noise photons N_b transmitted to the quantum detectors. In a system design, the field stop should be made sufficiently large to minimize losses to the quantum signal but otherwise made small enough to minimize the transmission of sky-noise photons. The choice of field stop size is closely tied to the

choice of quantum-signal wavelength, making wavelength perhaps the most critical design criterion. Still, the community has not settled on an ideal free-space quantum communication wavelength. For example, wavelengths of interest for satellite-Earth quantum communication have included both the 1550-nm telecom wavelength and

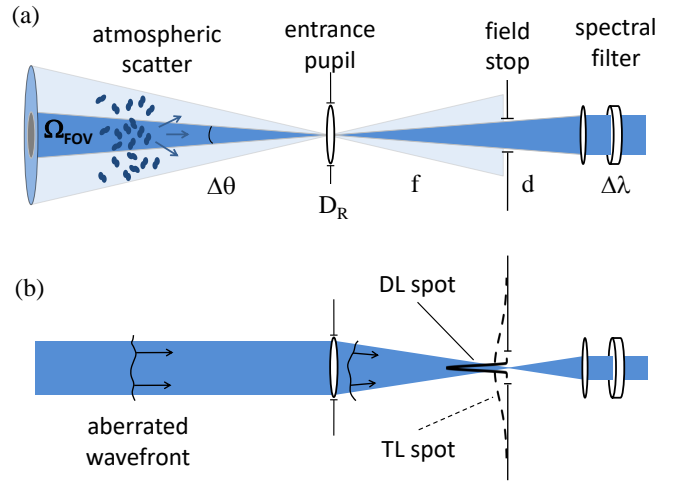


FIG. 1: Schematic illustrating (a) the concept of spatially filtering sky-noise photons created by atmospheric scattering. An entrance pupil D_R with focal length f and a field stop with diameter d determine the solid-angle FOV Ω_{FOV} . Reducing the FOV of the receiver can reduce the number of sky noise-photons transmitted to the spectral filter $\Delta\lambda$. Schematic (b) illustrates the effect of focusing in the presence of turbulence, that is, the aberrated wavefront results in a broadened turbulence-limited spot (TL spot) as compared to the diffraction-limited spot (DL spot).

* robert.lanning@us.af.mil

Approved for public release; distribution is unlimited. Public Affairs release approval AFRL-2021-0775.

shorter wavelengths near 775-nm [7, 13–15, 20, 21]. To date, most daytime free-space quantum-communication demonstrations have included rudimentary analysis on the wavelength dependence of quantum communication. For example, some have concluded that 1550-nm is ideal due to lower solar radiance, the wavelength-dependent nature of scattering, and compatibility with current telecom technology [16]. However, in this case they did not consider the effects of geometric coupling, spatial filtering strategies, or the wavelength dependence of the focused spot size as we do in this article. Furthermore, in the context of the global-scale quantum internet, we are at the stage of needing careful analyses that are linked to actual space-Earth channel atmospheric parameters and can help guide system development.

To analyze the wavelength-dependence of free-space quantum communication, we choose the decoy-state BB84 Quantum Key Distribution (QKD) [22, 23] bit yield as our performance metric. We simulate a satellite down-link scenario in the presence of daytime spectral radiance and atmospheric turbulence characterized by the Fried coherence length [24]. The Fried coherence length characterizes the dominating phenomenon determining the signal throughput at the receiver field stop. Except in the case of deep turbulence, which corresponds to large zenith angles or long horizontal propagation in a terrestrial link, scintillation presents a relatively small contribution to receiver performance [13, 14], and this translates to negligible effects on error and key rates of BB84-QKD over many space-Earth link scenarios [25]. Thus, scintillation will be neglected and we will derive the bit yield as a function of wavelength and spatial coherence, and investigate two different spatial filtering strategies.

We show that shorter wavelengths generally outperform longer wavelengths. We also investigate how site-specific atmospheric conditions can affect spectral filtering requirements. We show that more aggressive spectral filtering can be used to mitigate the effects of a more challenging atmosphere while still taking advantage of the optimal spatial filtering and aperture coupling for shorter wavelengths. We also cast the optimization problem in terms of higher-order Adaptive Optics (AO). Although realistic daytime atmospheres will be quite challenging, AO technology allows one to correct for atmospheric turbulence and in effect operate their optical receiver closer to the diffraction limit (see Fig. 1(b)). This allows one to use very tight spatial filtering and relax other filtering requirements if necessary [13–15]. AO will likely be necessary for high-performance entanglement-based protocols where narrow spectral filtering would significantly block the quantum signal. Therefore, our results represent a framework for designing free-space quantum-networking systems including specifying the optimal wavelength and the necessary filtering to achieve high performance.

II. THEORY

In this section we develop the theory necessary for establishing QKD bit yield as a performance metric. We progress in a pedagogic way, examining the wavelength dependence of each component contributing to the key bit yield. We define a low-Earth-orbit (LEO) satellite down-link architecture similar to our earlier numerical and experimental simulations demonstrating the benefits of AO [14, 15, 19]. We assume a 10-cm transmitter in a 600-km LEO and a 1-m ground receiver with efficiency $\eta_{\text{rec}} = 0.5$ and spectral filter efficiency $\eta_{\text{spec}} = 0.9$. Due to advances in superconducting nanowire single-photon detector technology, we show no partiality and assume detector efficiency $\eta_{\text{det}} = 0.8$ and detector dark count rate $f_{\text{dark}} = 10$ -Hz for all wavelengths. The signal pulse rate R_p is assumed to be 10-MHz, and the spectral/temporal filters are chosen to be 1-nm and 1-ns, respectively. Additional constants must be set in order to discuss the QKD protocol, specifically, we assume that the system noise error rate is $e_0 = 0.5$, the polarization cross-talk error is $e_d = 0.01$, and the error correction efficiency is $f_{\text{ec}} = 1.22$. Under a majority of the channel conditions we consider, we find that the optimal signal/decoy-state Mean Photon Number (MPN) are $\mu = 0.7$ and $\nu = 0.1$, respectively.

Using MODTRAN, we generate wavelength dependent transmission and spectral radiance profiles for different site-dependent downlink scenarios, that is, for a ground receiver looking to different points in the sky, with varying sun locations. In the foothills of the Manzano mountains outside Albuquerque NM, we experience an arid high-desert climate with desert albedos and urban aerosols. For example, in Fig. 2 we plot the atmospheric transmission and spectral radiance for a receiver pointed at zenith on winter solstice at 1:00 PM with 50-km visibility and we will use this site condition for the rest of the plots in this section. Considering the fine structure of the atmospheric transmission and spectral profiles is a critical step of the optimization problem. In a system design analysis, the fine spectral structure, that is, Fraunhofer lines, should be included around the target wavelength. For example, whereas the spectral radiance is relatively constant near 1550-nm, we judiciously chose dips in radiance near 780- and 430-nm to analyze in this section. Specifically, we will use 1549.91-, 780.945-, and 430.886-nm, but hereafter we will round to the nearest nanometer when discussing these wavelengths.

A. Spatial Filtering

The performance of a free-space QKD system ultimately depends on the amount of signal and noise that passes through the receiver field stop. Therefore, we will first introduce the physics related to the focused spot size and how this relates to field stop spatial-filtering strategies. As one might expect, these choices permeate

throughout the calculation and we will show how they effect the channel efficiency, noise probability, signal-to-noise and error rate.

For a receiver with no central obscuration operating at the diffraction limit, one can set the field stop to transmit the central peak of the diffraction limited Airy pattern, thus transmitting 84% of the signal light. Accordingly, the spatial filter diameter is

$$d_{\text{spot}}^{(\text{DL})} = 2.44 \frac{\lambda f}{D_{\text{R}}}, \quad (1)$$

where f is the receiver focal length and D_{R} is the receiver aperture diameter. This choice of spatial filter diameter gives the Diffraction Limited (DL) solid-angle FOV

$$\Omega_{\text{FOV}}^{(\text{DL})} = \pi \left(\frac{1.22\lambda}{D_{\text{R}}} \right)^2. \quad (2)$$

The solid lines in Fig. 3 give the solid-angle DL FOV $\Omega_{\text{FOV}}^{(\text{DL})}$ for 1550-, 781-, and 431-nm (black, red, and blue respectively). One can see, for example, that 1550-nm has $\sim 13\times$ larger FOV than 431-nm. Therefore, although the sky tends to be much brighter at shorter wavelengths (see Fig. 2(b)), a receiver operating near the diffraction

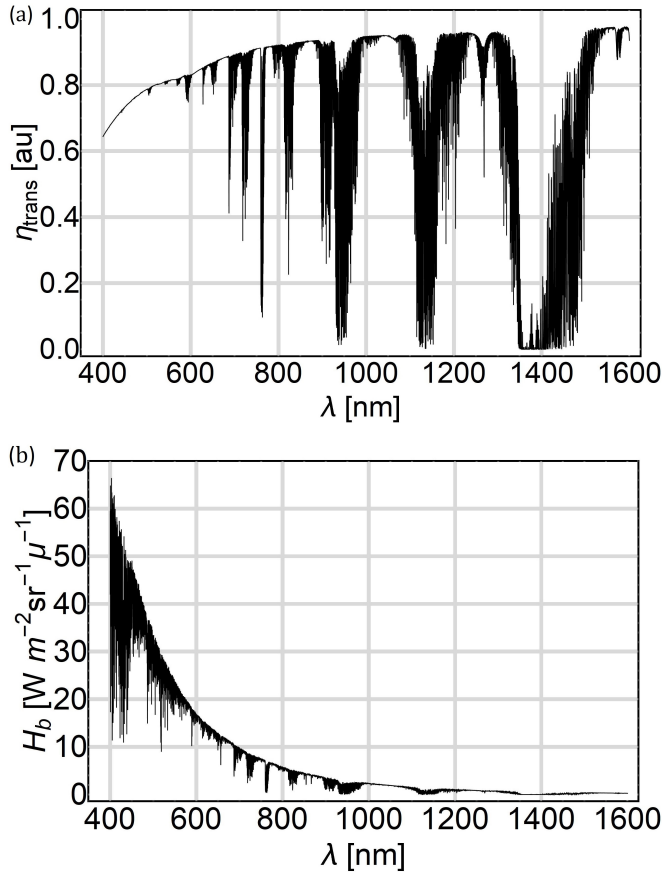


FIG. 2: The (a) atmospheric transmission η_{trans} and (b) spectral radiance H_{b} for a receiver pointed at zenith on winter solstice at 1:00 PM with 50-km visibility.

limit would be much more restrictive of that noise. This is the first of many competing phenomenon that are inherent to the optimal-wavelength problem, and this is further complicated when considering the effects of turbulence.

In the presence of turbulence, the lack of spatial coherence across the entrance pupil can inhibit an optical receiver's ability to focus the received light, in effect creating a broadened spot size (see Fig. 1(b)). The so-called Turbulence Limited (TL) spot size can be approximated by [26]

$$d_{\text{spot}}^{(\text{TL})} = d_{\text{spot}}^{(\text{DL})} / \sqrt{S}, \quad (3)$$

where

$$S = \left[1 + \left(\frac{D_{\text{R}}}{r(\lambda)} \right)^{5/3} \right]^{-6/5} \quad (4)$$

is the on-axis Strehl ratio, that is, the ratio of the aberrated- to DL-spot peak intensities,

$$r(\lambda) = r_0 (\lambda/500)^{6/5} \quad (5)$$

is the Fried coherence length, λ is the wavelength given in nanometers, and r_0 is the value measured at 500-nm [27]. Throughout this article, the symbol r_0 specifies the value of the Fried coherence length at 500-nm and can be considered a wavelength independent measure of the strength of turbulence. Choosing a spatial filter corresponding to the broadened spot size in Eq. 3 leads to the so-called TL solid-angle FOV

$$\Omega_{\text{FOV}}^{(\text{TL})} = \pi \left(1.22 \frac{\lambda}{D_{\text{R}}} \left[1 + \left(\frac{D_{\text{R}}}{r(\lambda)} \right)^{5/3} \right]^{3/5} \right)^2. \quad (6)$$

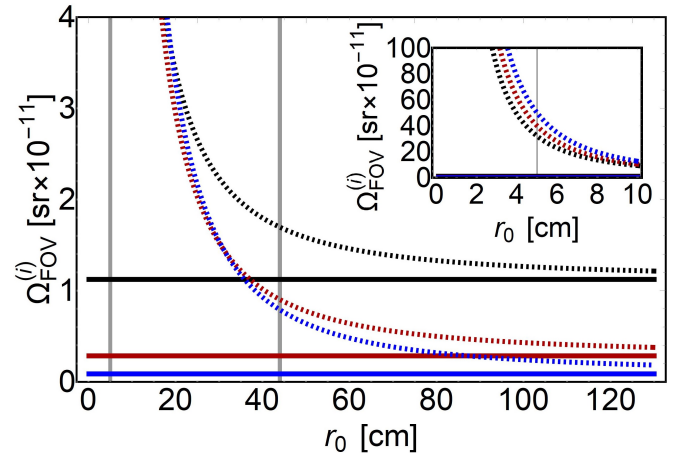


FIG. 3: Solid-angle field of view $\Omega_{\text{FOV}}^{(i)}$ for 1550-, 781-, and 431-nm (black, red, and blue respectively), plotted as a function of r_0 at 500-nm. The solid and dashed curves indicate the DL and TL FOVs, respectively. The vertical lines at $r_0^{(\text{OL})} = 5$ -cm and $r_0^{(\text{CL})} = 44$ -cm indicate effective r_0 corresponding to an example of open- and closed-loop AO operation, respectively.

The dashed lines in Fig. 3 give the solid-angle TL FOV $\Omega_{\text{FOV}}^{(\text{TL})}(r_0)$ for 1550-, 781-, and 431-nm (black, red, and blue respectively). The wavelength dependence of the Fried coherence length $r(\lambda)$ introduces another critical phenomenon, that is, the perceived turbulence is more intense at shorter wavelengths. This can be observed by examining the wavelength dependence of the FOV. Although the DL FOV is much smaller for the shorter wavelength, we see that the TL FOV increases more rapidly as r_0 gets small with respect to the receiver aperture size, that is, as the spatial coherence deteriorates. For example, when $r_0 = 30$ -cm, the TL FOV is $\sim 18\times$ larger than the DL FOV at 431-nm, but only $\sim 2\times$ larger at 1550-nm.

In Fig. 3 we plot a wide range of r_0 's to show the trend in $\Omega_{\text{FOV}}^{(\text{TL})}$ as the spatial coherence approaches the 1-m receiver diameter. However, realistic conditions will likely range from $5\text{-cm} < r_0 < 15\text{-cm}$. For example, assuming a Hufnagel-Valley (HV_{5/7}) [28] turbulence profile, we find a spatial coherence of $r_0 \equiv r(500\text{-nm}) \approx 5\text{-cm}$ (see App. A and Ref. [19] for more details). For reference, in this plot and throughout the article, we include vertical lines which indicate the r_0 's for a higher-order AO system operating in both the open- and closed-loop configuration. In a higher-order AO system, the aberrations of the incoming wavefront are corrected via a deformable mirror (DM) imprinted with the conjugate of the wavefront error. In the open-loop configuration the DM is flat, thus we assume $r_0^{(\text{OL})} = 5\text{-cm}$. In practice one would build a an AO system that is on the order of or several times faster than the temporal component of the turbulence. However, for this simulation we assume the same closed-loop bandwidth as the system we built for our field experiment reported in Ref. [19]. Despite this system only being designed to compensate for turbulence observed in a 1.6-km horizontal channel with stationary transmit/receive stations, we show that it could provide a relevant performance increase even if used in a space-Earth down-link architecture where slewing substantially increases the temporal atmospheric fluctuations. Hence, assuming the closed-loop bandwidth $f_c = 130\text{-Hz}$, we calculate the effective closed-loop spatial coherence $r_0^{(\text{CL})} \approx 44\text{-cm}$ (see App. A 2). Interestingly, there is a linear relationship between f_c and $r_0^{(\text{CL})}$. Therefore, one can easily assess how increasing the closed-loop bandwidth increases QKD system performance.

Whereas the DL FOV is constant, the TL FOV is a function of r_0 and grows with increasing turbulence strength in order to maintain 84% transmission. Thus, the intersection with the vertical line at $r_0 = 44\text{-cm}$ indicates the TL FOV one could operate at with a 130-Hz AO system correcting for turbulence while slewing through zenith. In fact, in this case AO would allow one to make their FOV $\sim 19\times$ smaller at 1550-nm and $\sim 63\times$ smaller at 431-nm.

However, careful analysis is in order when considering the effects of AO compensation and it is misguided to try to make broad generalizations about the relative im-

provement. Nonetheless, strictly in the context of FOV, 431-nm appears to be the optimal choice when considering the benefit of AO. However, there are several more competing phenomenon that ultimately effect the QKD system performance. Therefore, in each of the subsequent subsections, one must pay careful attention to the wavelength and spatial filtering dependence of each contribution to the key bit yield. For more details about the competing phenomenon that effect the focused spot size and the FOV, see App. A 4.

In this article we will consider two spatial filtering strategies. The first strategy is to choose the FOV according to r_0 , for example, free-space coupling to detectors using a field stop diameter corresponding to the average spot size for ones site condition. The second strategy is to operate the receiver at the DL FOV regardless of r_0 ; this corresponds to, for example, coupling into single-mode fiber prior to detection. These two strategies are defined more rigorously in the following section where we introduce the channel efficiency and background probability.

B. Channel Efficiency

The geometric aperture-to-aperture coupling is approximated by the Gaussian beam equation [29]

$$\eta_{\text{geo}} = 1 - \exp\left(-\frac{1}{2} \frac{D_{\text{R}}^2}{w^2(\lambda, z)}\right), \quad (7)$$

where $w^2(\lambda) = w_0^2(1 + z^2/z_{\text{R}}^2(\lambda))$ is the waist function, $z_{\text{R}} = \pi w_0^2/\lambda$ Rayleigh range, and $w_0 = 0.7D_{\text{T}}/2$ is the waist of the signal beam. Aperture-to-aperture coupling loss due to turbulence-induced beam spreading is negligible in the down-link architecture [30]. Loss at the spatial filter is defined in terms of the two spatial-filtering strategies. The first strategy is to accommodate for the broadened spot and increase the size of the field stop to always pass 84% of the signal. The second strategy is to keep the size of the field stop at the diffraction limit regardless of the broadened spot size. In the later case, the turbulence broadened spot may be partially blocked by the field stop spatial filter. To model this we take the ratio of the spot-size areas and find

$$\begin{aligned} \eta_{\text{FS}}^{(\text{TL})}(r_0, \lambda) &= 0.84 \\ \eta_{\text{FS}}^{(\text{DL})}(r_0, \lambda) &= 0.84 \times S, \end{aligned} \quad (8)$$

where S is defined in Eq. 4. These allow us to define the total channel efficiency

$$\begin{aligned} \eta^{(i)}(r_0, \lambda) &= \eta_{\text{geo}}(\lambda) \eta_{\text{trans}}(\lambda) \eta_{\text{FS}}^{(i)}(r_0, \lambda) \\ &\quad \times \eta_{\text{spec}} \eta_{\text{rec}} \eta_{\text{det}}, \end{aligned} \quad (9)$$

where i indicates either the DL or TL strategy, and η_{trans} is the atmospheric transmission efficiency predicted by MODTRAN and plotted in Fig. 2(b).

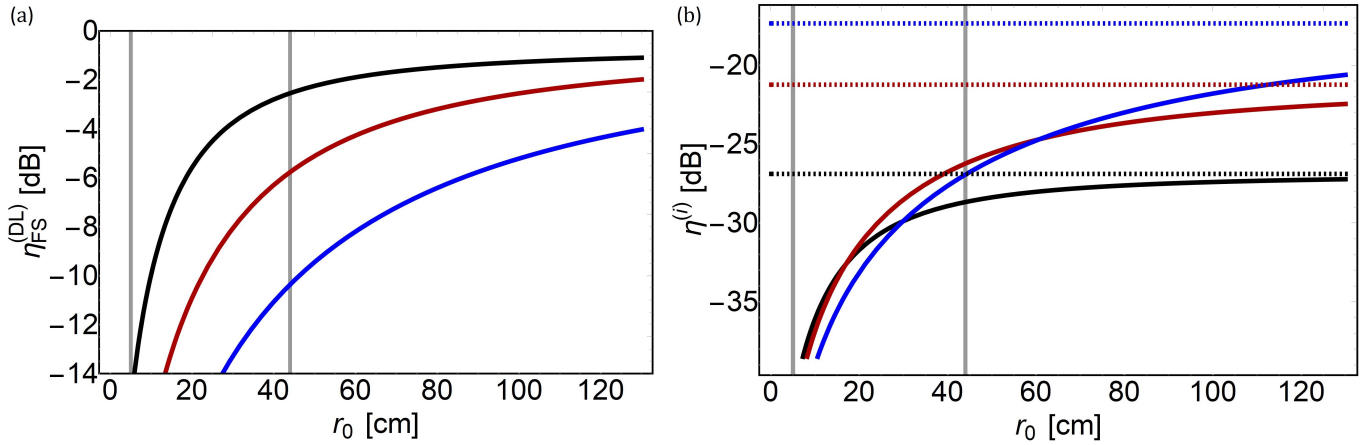


FIG. 4: The (a) DL strategy field stop transmission efficiency $\eta_{\text{FS}}^{(\text{DL})}$ and (b) total system efficiency $\eta^{(\text{DL})}$ for 1550-, 781-, and 431-nm (black, red, and blue respectively), plotted as a function of r_0 at 500-nm. The solid and dashed curves indicate the DL and TL strategies, respectively. The vertical lines at $r_0^{(\text{OL})} = 5\text{-cm}$ and $r_0^{(\text{CL})} = 44\text{-cm}$ indicate the effective r_0 corresponding to an example of open- and closed-loop AO operation, respectively.

In Fig. 4 we plot the r_0 dependence of $\eta_{\text{FS}}^{(\text{DL})}$ and $\eta^{(i)}$ for 1550-, 781-, and 431-nm (black, red, and blue respectively). Figure 4(a) shows the r_0 dependence of the field stop transmission which reveals the wavelength dependent nature of focusing in the presence of turbulence, that is, the effects of turbulence are weaker at longer wavelengths and 1550-nm appears to have the advantage. Again, the intersections with the vertical lines at $r_0^{(\text{OL})} = 5\text{-cm}$ and $r_0^{(\text{CL})} = 44\text{-cm}$ indicate the achievable channel efficiency for a specific example of open- and closed-loop AO operation, respectively.

Figure 4(b) shows the r_0 dependence of the total system transmission which reveals the limitation of longer wavelengths, that is, the geometric coupling prevails and lends an advantage to the shorter wavelengths. Thus, we see that despite the relatively low efficiency at the field stop, with AO correction the total channel efficiencies are actually higher for 431- and 781-nm. Figure 4(b) also serves as an illustration of the two field stop strategies. For example, $\eta^{(\text{TL})}$ is constant over the entire range of r_0 while $\eta^{(\text{DL})}$ decreases once the lack of spatial coherence begins to broaden the spot size for the specified wavelength. One might realize the benefit of the TL strategy if their site conditions are relatively constant in r_0 , or more ambitiously, by developing higher-order AO systems with adaptive spatial-filters, that is, a spatial filter that adjusts according to the effective r_0 of the AO system, thereby dynamically maximizing signal throughput and maintaining noise filtering at the field stop.

C. Background Probability

For either strategy, the number of noise photons transmitted by the field stop within a time, wavelength, and

FOV window is given by the radiometric equation

$$N_b^{(i)} = \int d\lambda \frac{\lambda}{hc} H_b(\lambda) \Omega_{\text{FOV}}^{(i)}(r_0, \lambda_0) \pi D_R^2 \Delta t, \quad (10)$$

where the integral is performed over a notch filter with width $\Delta\lambda$ and central wavelength λ_0 , the spectral radiance $H_b(\lambda)$ is predicted by MODTRAN and given in Fig. 2(b), Δt is the temporal detection window, h is Planck's constant, c is the speed of light, and i indicates either the DL or TL strategy. Comparing Fig. 5(a) and Fig. 2(b) reveals the effect of FOV and photon energy on the reduction of the number of photons at shorter wavelengths. For example, under the atmospheric conditions assumed in this section the sky is approximately 20 times brighter at 781-nm as compared to 1550-nm, but there are only 2.5 times the number photons for the DL strategy. This reduction in number of photons is a result of the higher photon energy hc/λ and the more effective spatial filtering for the shorter wavelengths, that is, the smaller FOV as a consequence of the λ^2 dependence of Eq. 1. One should note that the relative brightness is highly dependent on site conditions. For example, in Sec. 3 we discuss how lower visibility conditions close the gap in relative brightness.

Figure 5(b) reveals the negative effects of widening the FOV with the TL strategy by giving the r_0 dependence of $N_b^{(i)}$ for 1550-, 781-, and 431-nm. For example, when $r_0 \approx 44\text{-cm}$, $N_b^{(\text{TL})}(431\text{-nm})$ is approximately 9 times greater than $N_b^{(\text{DL})}(431\text{-nm})$. This might suggest that the TL strategy is fundamentally flawed due to the excess noise, but it also accommodates a boost in signal due to the optimal channel efficiency. Therefore, the question which remains to be answered is whether the excess noise actually translates to increased errors and lower QKD system performance. In the following, we reveal the performance of the TL strategy by investigating

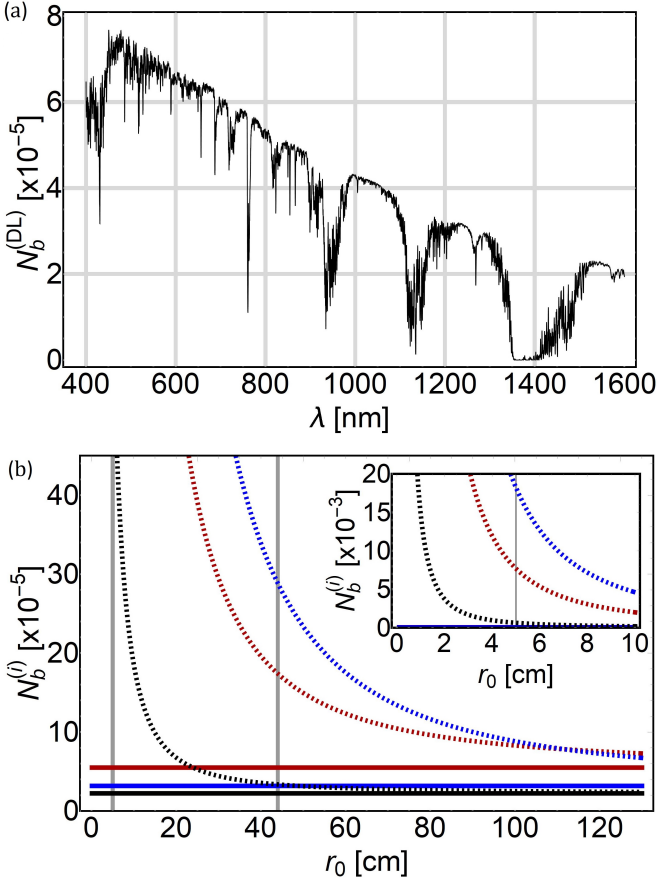


FIG. 5: The (a) wavelength dependence of the number of background photons for the DL strategy $N_b^{(\text{DL})}$ and (b) the r_0 dependence of $N_b^{(i)}$ for 1550-, 781-, and 431-nm (black, red, and blue respectively), plotted as a function of r_0 at 500-nm. In (b), the solid and dashed curves indicate the DL and TL strategies, respectively. The vertical lines at $r_0^{(\text{OL})} = 5$ -cm and $r_0^{(\text{CL})} = 44$ -cm indicate the effective r_0 corresponding to an example of open- and closed-loop AO operation, respectively.

the error rate, signal-to-noise, and ultimately the key-bit probability. To do so we must define the background probability [23]

$$Y_0^{(i)}(r_0, \lambda) = N_b^{(i)}(r_0, \lambda) \eta_{\text{spec}} \eta_{\text{rec}} \eta_{\text{det}} + 4f_{\text{dark}} \Delta t, \quad (11)$$

which has a contribution from the detector dark counts, but is dominated by the number of photons $N_b^{(i)}$ and the choice of strategy.

D. Quantum Bit Error Rate

Next, we define the decoy/signal Quantum Bit Error Rate (QBER) [23]

$$E_{r,n}^{(i)}(r_0, \lambda) = \frac{e_0 Y_0^{(i)}(r_0, \lambda) + e_d (1 - e^{-\eta^{(i)}(r_0, \lambda) n})}{Y_0^{(i)}(r_0, \lambda) + 1 - e^{-\eta^{(i)}(r_0, \lambda) n}}, \quad (12)$$

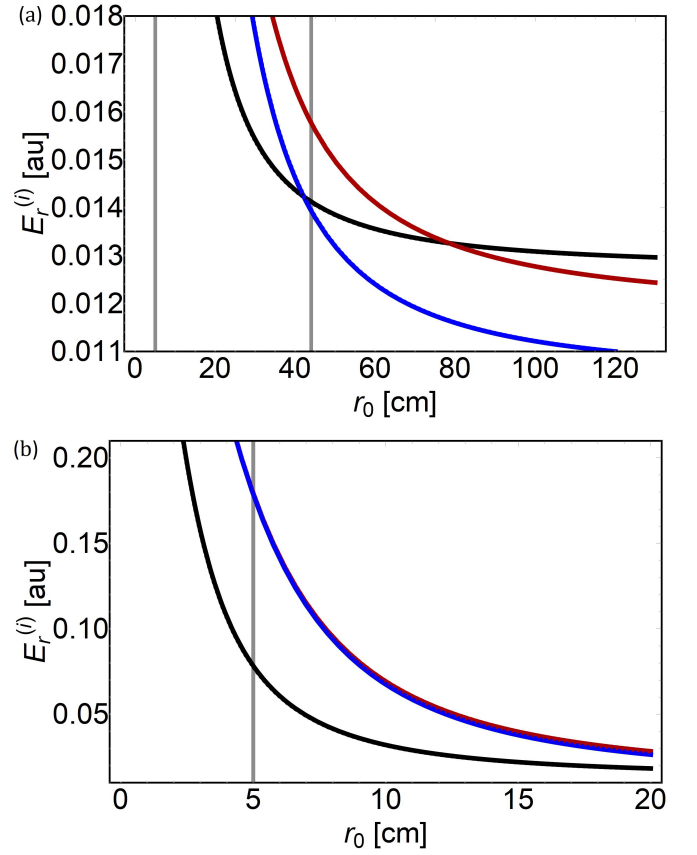


FIG. 6: The r_0 (at 500-nm) dependence of $E_r^{(i)}$ for 1550-, 781-, and 431-nm (black, red, and blue respectively). The solid and dashed curves indicate the DL and TL strategies, respectively. In (a) the vertical lines at $r_0^{(\text{OL})} = 5$ -cm and $r_0^{(\text{CL})} = 44$ -cm indicate the effective r_0 corresponding to an example of open- and closed-loop AO operation, respectively. In (b) we plot the range of r_0 representative of no AO correction.

where n is the MPN of the signal or decoy state. In Fig. 6(a) and 6(b) we plot the r_0 dependence of $E_{r,\mu}^{(i)}$ for 1550-, 781-, and 431-nm and two different ranges of r_0 . Interestingly, despite $N_b^{(i)}(\lambda)$ (and correspondingly $Y_0^{(i)}(\lambda)$) being larger for the TL strategy, the QBERs are practically indistinguishable. This is because the probability of detecting a signal photon $1 - e^{-\eta^{(i)}(r_0, \lambda) \mu}$ also increases with the TL strategy. Apparently, the increase in noise is directly compensated by the increase in signal, and in effect, the ratio in Eq. 12 remains nearly constant. This can be investigated by keeping the first term in the expansion of $1 - e^{-\eta^{(i)}(r_0, \lambda) \mu}$. Making this substitution in Eq. 12 and rearranging terms one can find that the QBER for DL strategy is

$$E_{r,n}^{(\text{DL})} \approx \frac{e_0 (Y_0^{(\text{TL})} + \epsilon) + e_d \eta^{(\text{TL})} n}{Y_0^{(\text{TL})} + \epsilon + \eta^{(\text{TL})} n}, \quad (13)$$

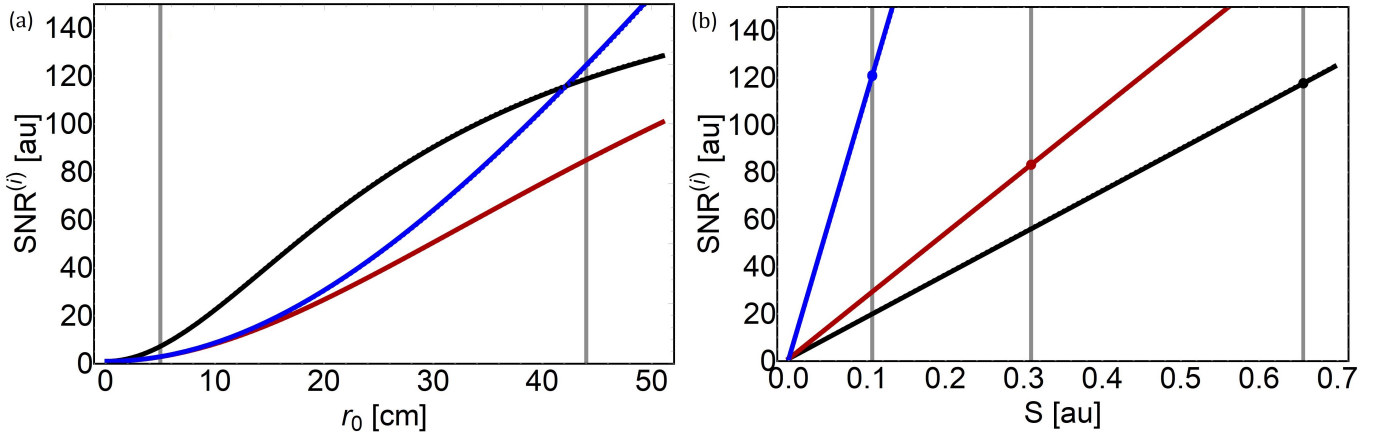


FIG. 7: The (a) r_0 (at 500-nm) and (b) S dependence of $SNR_\mu^{(i)}(\lambda)$ for 1550-, 781-, and 431-nm (black, red, and blue respectively). The solid and dashed curves indicate the DL and TL strategies, respectively. In (a) the vertical lines at $r_0^{(OL)} = 5$ -cm and $r_0^{(CL)} = 44$ -cm indicate the effective r_0 corresponding to an example of open- and closed-loop AO operation, respectively. In (b) the λ dependence of S produces three vertical lines indicating AO correction.

where $\epsilon \equiv 4f_{\text{dark}} \Delta t(1/S - 1)$. Therefore, we see that the functional dependence of the QBER for the TL and DL strategies differ by an additive noise term ϵ in the numerator and denominator. When $r(\lambda)$ increases relative to the receiver diameter D_R , the Strehl approaches unity, the noise term $\epsilon \rightarrow 0$, and $E_{r,n}^{(DL)} = E_{r,n}^{(TL)}$. Fortunately, this noise term is always very small due to the dependence on the narrow temporal filtering Δt and low dark-count rate f_{dark} , and this explains the similar r_0 dependence of the QBER for the two strategies.

E. Signal-To-Noise

Next, we will investigate the Signal-to-Noise Ratio (SNR) which we define as the ratio of signal gain to background probability

$$SNR_n^{(i)}(r_0, \lambda) = Q_n^{(i)}(r_0, \lambda) / Y_0^{(i)}(r_0, \lambda), \quad (14)$$

where

$$Q_n^{(i)}(r_0, \lambda) = Y_0^{(i)}(r_0, \lambda) + 1 - e^{-\eta^{(i)}(r_0, \lambda)n}, \quad (15)$$

is the signal/decoy state gain [23]. In Fig. 7(a) we plot the r_0 dependence of $SNR_\mu^{(i)}$ for 1550-, 781-, and 431-nm. Similar to the QBER, we do not see a significant difference between the two strategies, thus confirming the relationship between the signal and noise for the TL strategy. To reiterate, the TL strategy accommodates a proportional boost in signal and noise in such a way as to not increase the error rate.

It is also useful to investigate the SNR as a function of Strehl via the relation in Eq. 4. In Fig. 7(b) we see that 431-nm outperforms the longer wavelengths for all values of Strehl. Since Strehl is a function of r_0 and λ , we now

have three separate vertical lines indicating QKD system performance with AO correction (see App A 3). In effect, a given AO correction yields a lower Strehl for the shorter wavelengths. For this reason it might be tempting to assume that the longer wavelengths will yield better QKD system performance. Strictly in terms of the SNR of a system with AO correction, we see that the longer wavelengths have much better Strehl, but the SNR can be higher at 431-nm due to the low relative noise as is evident by the low QBER (see Fig. 6(a) at $r_0^{(CL)}$). The SNR helps build intuition regarding the performance of different wavelengths, but ultimately one must adopt a quantum metric to make any legitimate claim. Therefore, we will now investigate the KBP and reveal how the wavelength dependent trends in channel efficiency, QBER, and SNR translate to actual QKD system performance.

F. Key Bit Rate

To establish the Key Bit Probability (KBP) we must define a few more important quantities [23]. Although these are well known, we include them here for completeness and convenience. The single photon gain is

$$Q_1^{(i)}(r_0, \lambda) = \frac{\mu^2 e^{-\mu}}{\mu\nu - \nu^2} \left(Q_\nu^{(i)}(r_0, \lambda) e^\nu - Q_\mu^{(i)}(r_0, \lambda) e^\mu \frac{\nu^2}{\mu^2} - \frac{\mu^2 - \nu^2}{\mu^2} Y_0^{(i)}(r_0, \lambda) \right), \quad (16)$$

and similarly the single photon state yield is

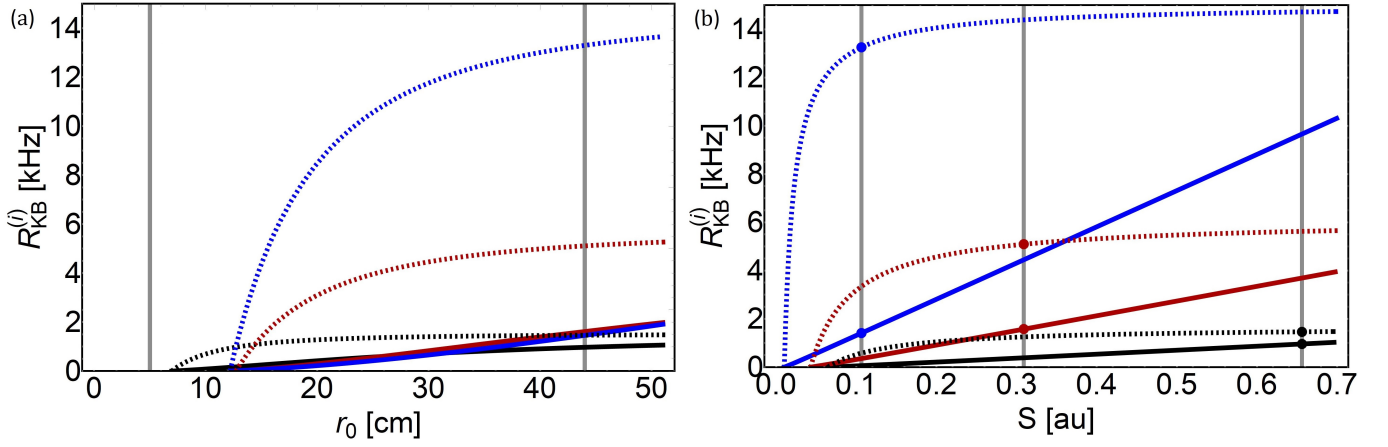


FIG. 8: The (a) r_0 and (b) S dependence of the key rate $R_{\text{KB}}^{(i)}$ for 1550-, 781-, and 431-nm (black, red, and blue respectively). The solid and dashed curves indicate the DL and TL strategies, respectively. In (a) the vertical lines at $r_0^{(\text{OL})} = 5\text{-cm}$ and $r_0^{(\text{CL})} = 44\text{-cm}$ indicate the effective r_0 corresponding to an example of open- and closed-loop AO operation, respectively. In (b) the λ dependence of S produces three vertical lines indicating AO correction.

$$Y_1^{(i)}(r_0, \lambda) = \frac{\mu}{\mu\nu - \nu^2} \left(Q_\nu^{(i)}(r_0, \lambda) e^\nu - Q_\mu^{(i)}(r_0, \lambda) e^\mu \frac{\nu^2}{\mu^2} - \frac{\mu^2 - \nu^2}{\mu^2} Y_0^{(i)}(r_0, \lambda) \right). \quad (17)$$

Lastly, the single photon state error rate is

$$e_1^{(i)}(r_0, \lambda) = \frac{E_{r,\nu}^{(i)}(r_0, \lambda) Q_\nu^{(i)}(r_0, \lambda) e^\nu}{Y_1^{(i)}(r_0, \lambda) \nu} - \frac{e_0 Y_0^{(i)}(r_0, \lambda)}{Y_1^{(i)}(r_0, \lambda) \nu}. \quad (18)$$

Finally, we define the KBP [23]

$$P_{\text{KB}}^{(i)}(r_0, \lambda) = \frac{1}{2} \left(-Q_\mu^{(i)}(r_0, \lambda) f_{ec} H_2[E_{r,\mu}^{(i)}(r_0, \lambda)] + Q_1^{(i)}(r_0, \lambda) (1 - H_2[e_1^{(i)}(r_0, \lambda)]) \right), \quad (19)$$

where $H_2(x) = -x \log_2(x) - (1-x) \log_2(1-x)$ is the Shannon binary entropy formula. The KBP is used to define the key rate

$$R_{\text{KB}}^{(i)}(r_0, \lambda) = R_p (1 - N_{\nu\mu}) P_{\text{SKB}}^{(i)}(r_0, \lambda), \quad (20)$$

where $N_{\nu\mu} = 3/10$ is the ratio of decoy plus vacuum pulses.

In Fig. 8(a) we plot the key rate as a function of r_0 . Interestingly, despite the two FOV strategies yielding nearly identical results for QBER and SNR, we see a drastic difference when examining the key rate. As compared to the DL strategy, the TL strategy experiences a dramatic increase in key rate for challenging r_0 's. This is because, quite fortuitously, the TL strategy permits a large boost in signal gain Q_μ without any significant boost in QBER. Another striking feature is the relatively

high performance of the shorter wavelengths. Despite turbulence effects being weaker and the sky being dimmer at 1550-nm, one can see that 781- and 431-nm perform better for $r_0 > 13\text{-cm}$. The only scenario where 1550-nm is a reasonable option is when $r_0 < 13\text{-cm}$ and narrower filtering spatial, spectral, or temporal filtering are not viable options.

To investigate the relatively high performance of the TL FOV strategy one can rearrange Eq. 19 and find

$$P_{\text{KB}}^{(i)}(r_0, \lambda) = \frac{1}{2} Q_\mu^{(i)}(r_0, \lambda) \left(-c_1^{(i)}(r_0, \lambda) + q^{(i)}(r_0, \lambda) c_2^{(i)}(r_0, \lambda) \right), \quad (21)$$

where

$$\begin{aligned} q^{(i)}(r_0, \lambda) &= Q_1^{(i)}(r_0, \lambda) / Q_\mu^{(i)}(r_0, \lambda) \\ c_1^{(i)}(r_0, \lambda) &= f_{ec} H_2[E_{r,\mu}^{(i)}(r_0, \lambda)] \\ c_2^{(i)}(r_0, \lambda) &= (1 - H_2[e_1^{(i)}(r_0, \lambda)]). \end{aligned} \quad (22)$$

The ratio of gains $q^{(i)}$ remains relatively constant upon switching between the filtering strategies because the fractional loss induced by the field stop does not effect single- and multi-photon pulses differently at such low MPNs and channel efficiencies. Furthermore, $c_1^{(i)}$ and $c_2^{(i)}$ remain relatively constant by virtue of the behavior of the error rates $E_{r,\mu}^{(i)}$ and $e_1^{(i)}$, respectively. Therefore, the dominating trend in the Eq. 21 comes from the leading factor $Q_\mu^{(i)}$. In Fig. 4 we showed how loss at the spatial filter significantly reduces the channel efficiency for the DL strategy with respect to the TL strategy. In Fig. 9 we show how this effects the signal gain by plotting the ratio $Q_\mu^{(\text{TL})} / Q_\mu^{(\text{DL})}$ as a function of r_0 for 1550-, 781-, and 431-nm. This clearly shows the drastic improvement

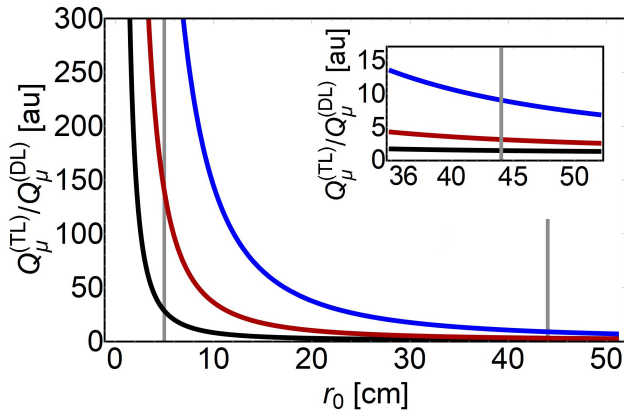


FIG. 9: The ratio $Q_\mu^{(\text{TL})}/Q_\mu^{(\text{DL})}$ for 1550-, 781-, and 431-nm (black, red, and blue respectively), plotted as a function of r_0 at 500-nm. The solid and dashed curves indicate the DL and TL strategies, respectively. The vertical lines at $r_0^{(\text{OL})} = 5\text{-cm}$ and $r_0^{(\text{CL})} = 44\text{-cm}$ indicate the effective r_0 corresponding to an example of open- and closed-loop AO operation, respectively.

in signal gain for small r_0 and the TL strategy. This effect, in conjunction with Eq. 21, reveals how the TL strategy permits such relatively high performance.

The vertical line at 5-cm in Fig. 8(a) reveals that none of the wavelengths could generate key bits under the current atmospheric and system conditions. To increase performance, one has no choice but to implement some form of more aggressive noise filtering. For example, the vertical line $r_0 = 44\text{-cm}$ reveals the key rates attainable with higher-order AO and correspondingly tighter spatial filtering. One can see that 431-nm and the TL strategy is the optimal choice giving more than a $9\times$ improvement over 1550-nm. In fact, we judiciously chose 431-nm because it gives the largest key rate in the 400- to 1600-nm range when using a 1-nm filter (see App B). For reference, this level of performance is comparable to a system without AO compensation but utilizing a much narrower $\Delta\lambda=0.05\text{-nm}$ filter.

In the case of AO, our simulation shows that high QKD performance can be achieved with relatively low system Strehls. This is somewhat counterintuitive since it is customary to relate system Strehl to system performance. However, in Fig. 8(b) we see that with the TL strategy and a corrected Strehl near 0.1, high performance can be achieved at 431-nm, in effect beating a 1550-nm system operating at the diffraction limit by a factor of ~ 9 . Moreover, for a 431-nm system, a majority of the TL strategy performance is achievable with a low Strehl, that is, with a Strehl of 0.1, one can achieve $\sim 90\%$ of the maximum key rate at that wavelength. This is in contrast to a 1550-nm system that only achieves $\sim 34\%$ of the maximum key rate at a Strehl of 0.1. Next we will discuss how these effects relate to the speed of the AO system.

As we outlined in App A, the amount of AO correction ultimately depends on the ability of the AO sys-

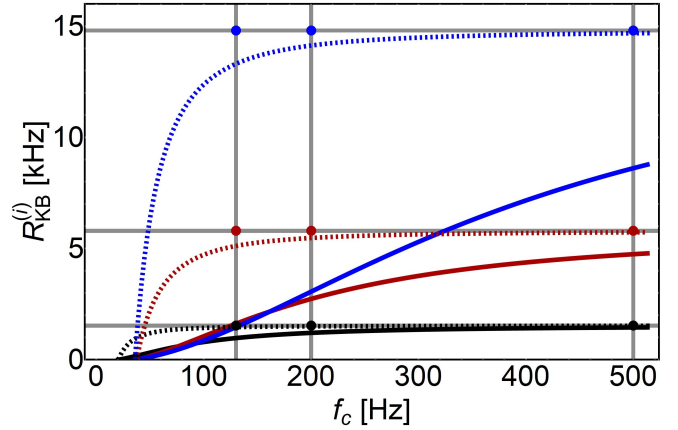


FIG. 10: The closed-loop bandwidth f_c dependence of the key rate $R_{\text{KB}}^{(i)}$ for 1550-, 781-, and 431-nm (black, red, and blue respectively). The solid and dashed curves indicate the DL and TL strategies, respectively.

The vertical line at $f_c = 130\text{-Hz}$ indicates the closed-loop bandwidth of the system built for our field experiment [19] whereas $f_c = 200\text{-}$ and 500-Hz indicate bandwidths assumed in previous numerical simulations [14, 15]. The horizontal lines indicate the maximum key rate for each wavelength, that is, the key rate for the receiver operating at the diffraction limit.

tem to keep pace with the temporal component of atmospheric turbulence, that is, the Greenwood frequency f_G . However, once again, a naive analysis is very misleading. Similar to the Fried coherence length, the observed f_G is also worse at shorter wavelengths (see Eq. A3). For example, when $f_G(500\text{-nm})=300\text{-Hz}$, we find that $f_G(1550\text{-nm})\approx 77\text{-Hz}$ and $f_G(431\text{-nm})\approx 360\text{-Hz}$. Therefore, one might assume that an AO system will need to be faster to operate at 431-nm. However, in this study, we have kept the AO system closed-loop bandwidth (see Eq. A4) fixed at $f_c = 130\text{-Hz}$ regardless of wavelength, and relatively large KBP at 431-nm has nonetheless been revealed. Even more striking is that the AO system could even be considerably slower. It is apparent that high performance is observed even for a Strehl $S = 0.05$ at 431-nm. This actually corresponds to an AO system that is operating at only 64% the speed that has been assumed thus far. In fact, a system operating at 431-nm with the TL FOV and $f_c \sim 40\text{-Hz}$ could in principle outperform a 1550-nm system operating at the diffraction limit.

In Fig. 10 we plot the key rate as a function of the closed-loop bandwidth of the AO system. First, this plot illustrates a prevailing concept well understood in the AO community, that is, given a certain closed-loop bandwidth, the amount of wavefront correction will be better at longer wavelengths. This is evident from examining the solid DL-FOV-strategy curves in relation to that maximum key rate for $f_c = 500\text{-Hz}$. The 1550-nm system would be practically operating at the diffraction limit where as the 781- and 431-nm systems fall notice-

ably short of diffraction limited performance. This is evident from the gap between the solid curves and the respective dots indicating the max key rates for each of the wavelengths. On the other hand, this plot illustrates a less common concept, that is, perfect wavefront correction is not necessarily needed for high performance. The dashed TL-FOV-strategy curves show that with relatively slow AO, high performance can still be achieved despite the wider FOV. For example, at $f_c = 130$ -Hz, the key rate $R_{\text{KB}}^{(\text{TL})}(\lambda)$ is already quite close to the maximum key rate for each wavelength. Therefore, one should weigh the increased technological challenges faced when building a faster AO system with the diminishing returns evident when already using the TL FOV strategy. In the following section we will investigate how performance changes with more challenging atmospheric conditions, namely diminishing visibility on both winter and summer solstice, and explore how narrower spectral filtering can restore performance.

III. VISIBILITY STUDY

The parameter space of atmospheric conditions is seemingly infinite for the down-link scenario. However, many of the effects can be studied with relatively simple analyses. For our purposes here, it suffices to investigate the effects due to changes in visibility while at zenith. An angle dependent study would be redundant, except in the case of large zenith angles where effects due to scintillation may need to be included. This is because as zenith angle increases, the longer propagation path reduces transmission and increases scattering in the channel, but these are the same effects observed with decreased visibility. We will consider two sun positions, namely winter and summer solstices at 1:00PM.

A. Winter Solstice

In this subsection we consider medium (23-km) and low (5-km) visibilities on winter solstice (see Figs. 11(a-b) and 12(a-b), respectively). One will see that a lower visibility condition decreases the atmospheric transmission and correspondingly increases the spectral radiance due to increased scattering of sunlight. In Fig. 11(c-e) and 12(c-e) we plot the r_0 dependence of $R_{\text{KB}}^{(i)}$ for the two winter solstice visibility conditions. One will notice that the absence of intersections with the vertical line at $r_0=5$ -cm indicates that it is not possible to generate key with a large spectral filter and without AO compensation. With AO enabled, one will see that the relative high performance of shorter wavelengths and the TL strategy persists.

In Fig. 11(f) and 12(f) we plot $R_{\text{KB}}^{(i)}$ as a function of system Strehl. Analyzing the performance as a function of Strehl again reveals that a relatively slow AO sys-

tem would enable relatively high performance at shorter wavelengths. Comparing the two conditions, we see that the grouping at low Strehl in Fig. 11(f) is replaced with a more dispersed trend in Fig. 12(f). This is a result of the relative sky radiance at the two visibility conditions. For example, for medium visibility, 431-nm is $\sim 27\times$ brighter than 1550-nm, but only $\sim 10\times$ brighter for low visibility. When considering the actual *number* of photons, using the DL spatial filtering strategy and a 1-nm spectral filter, one finds that there are actually $\sim 1.2\times$ more 1550-nm photons at medium visibility and $\sim 3\times$ more at low visibility. In effect, the breakout in the curve is caused by the relatively larger QBER's at the longer wavelengths. This can be traced back to the issue between the FOV's of the different systems. The sky may be dimmer at 1550-nm, but a system at that wavelength is more susceptible to that noise as compared to shorter wavelengths. Therefore, this reveals further robustness of the short wavelength strategy under conditions where the relative sky brightness increases for longer wavelengths.

B. Summer Solstice

For summer solstice, since the sun is approximately 15-degrees from zenith, we will only consider high (50-km) and medium (23-km) visibilities. Thus far, we have assumed a relatively large 1-nm spectral filter for our down-link architecture. This emphasizes the robustness of particular wavelength and strategy choices, and also suggests the level of performance possible when using entangled photon sources with comparable bandwidth. However, in this case the spectral radiance is significantly larger due to the channel proximity to the sun and we would like to demonstrate the level of filtering necessary to generate key without the aid of AO. Therefore, we narrow the spectral filter to $\Delta\lambda = 0.05$ -nm for both visibility conditions. In practice, one should use the most aggressive filtering as possible and be careful to examine how the choice of filter affects the number of background photons within that spectral window $N_b(\lambda_0, \Delta\lambda)$ (see Eq. 10). In effect, the choice of filter and subsequent number of background photons can change the optimal wavelength for key generation. For example, reducing the filter from 1-nm to 0.05-nm takes advantage of a narrow dip in spectral radiance and causes the optimal wavelength to shift from 431-nm to near 405-nm (see App B). Therefore, in this subsection the blue curves correspond to 405-nm.

Figures 13(a-b) and 14(a-b) show the atmospheric transmission and spectral radiance for high and medium visibility, respectively. In Fig. 13(c-e) and 14(c-e) we plot the r_0 dependence of $R_{\text{KB}}^{(i)}$ for the two summer solstice visibility conditions. One will see that the spectral radiances are considerably higher as compared to the winter solstice condition. One will also notice the relative high performance of shorter wavelengths and the TL strategy, which persists even for more challenging atmospheric conditions. Interestingly, the tighter filtering permits

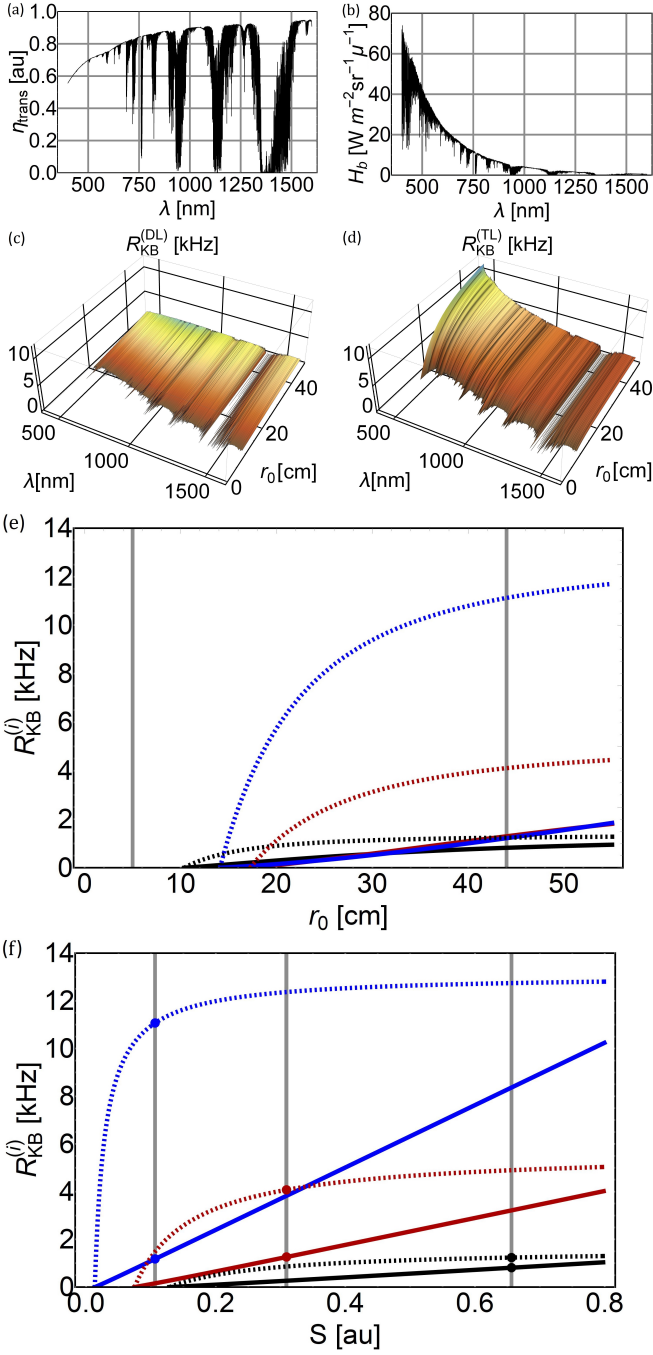


FIG. 11: The (a-b) atmospheric transmission η_{trans} and spectral radiance H_b , and (c-d) the secret key rate $R_{\text{KB}}^{(i)}$ for winter solstice with medium visibility (23-km), plotted as a function of r_0 at 500-nm. In (e-f) we have chosen 1550-, 781-, and 431-nm (black, red, and blue respectively), and the solid and dashed curves indicate the DL and TL strategies, respectively. In (e) the vertical lines at $r_0^{(\text{OL})} = 5$ -cm and $r_0^{(\text{CL})} = 44$ -cm indicate the effective r_0 corresponding to an example of open- and closed-loop AO operation, respectively. In (f) the λ dependence of S produces three vertical lines indicating AO correction.

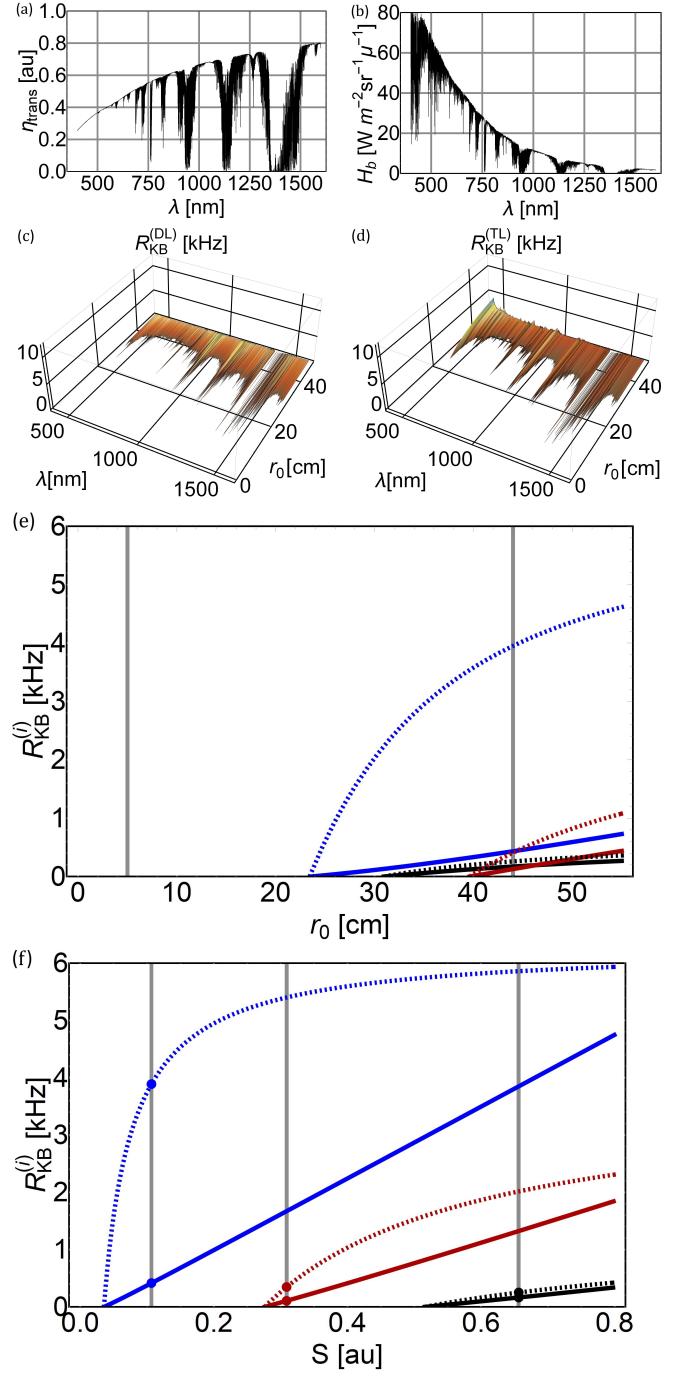


FIG. 12: The (a-b) atmospheric transmission η_{trans} and spectral radiance H_b , and (c-d) the secret key rate $R_{\text{KB}}^{(i)}$ for winter solstice with low visibility (5-km), plotted as a function of r_0 at 500-nm. In (e-f) we have chosen 1550-, 781-, and 431-nm (black, red, and blue respectively), and the solid and dashed curves indicate the DL and TL strategies, respectively. In (e) the vertical lines at $r_0^{(\text{OL})} = 5$ -cm and $r_0^{(\text{CL})} = 44$ -cm indicate the effective r_0 corresponding to an example of open- and closed-loop AO operation, respectively. In (f) the λ dependence of S produces three vertical lines indicating AO correction.

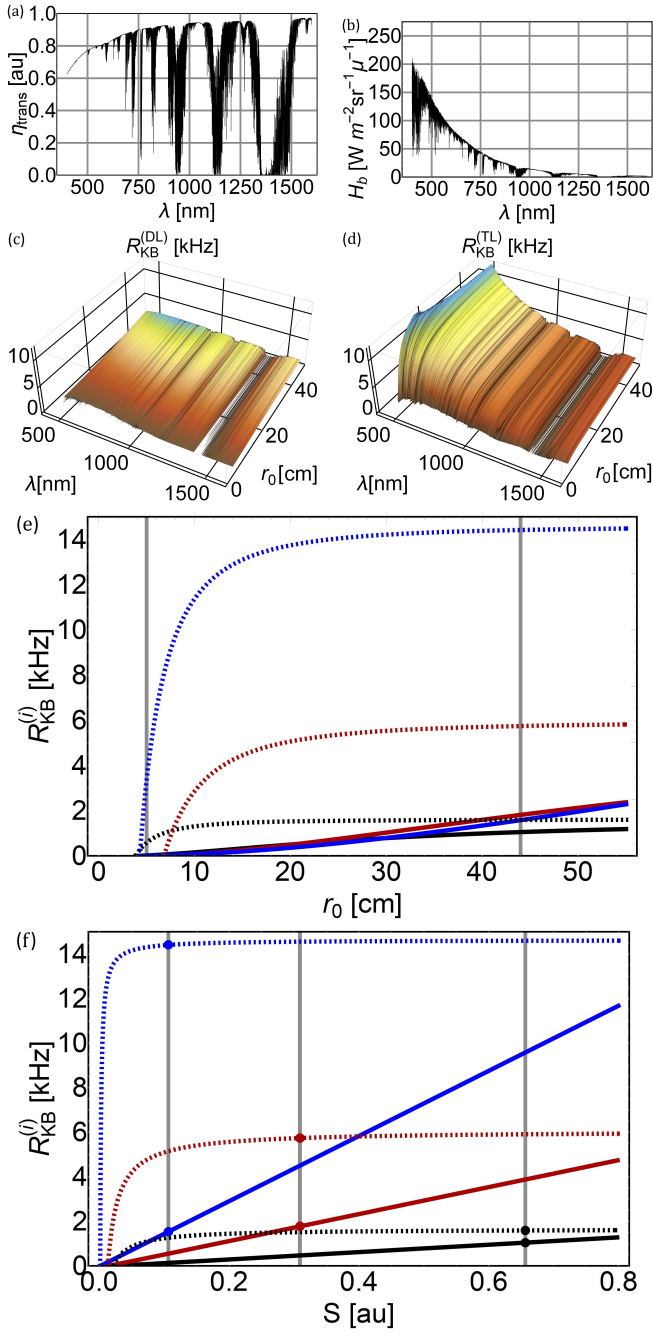


FIG. 13: The (a-b) atmospheric transmission η_{trans} and spectral radiance H_b , and (c-d) the secret key rate $R_{\text{KB}}^{(i)}$ for summer solstice with high visibility (50-km), plotted as a function of r_0 at 500-nm. In this case we have narrowed the spectral filter width to $\Delta\lambda = 0.05$ -nm. In (e-f) we have chosen 1550-, 781-, and 405-nm (black, red, and blue respectively), and the solid and dashed curves indicate the DL and TL strategies, respectively.

In (e) the vertical lines at $r_0^{(\text{OL})} = 5$ -cm and $r_0^{(\text{CL})} = 44$ -cm indicate the effective r_0 corresponding to an example of open- and closed-loop AO operation, respectively. In (f) the λ dependence of S produces three vertical lines indicating AO correction.

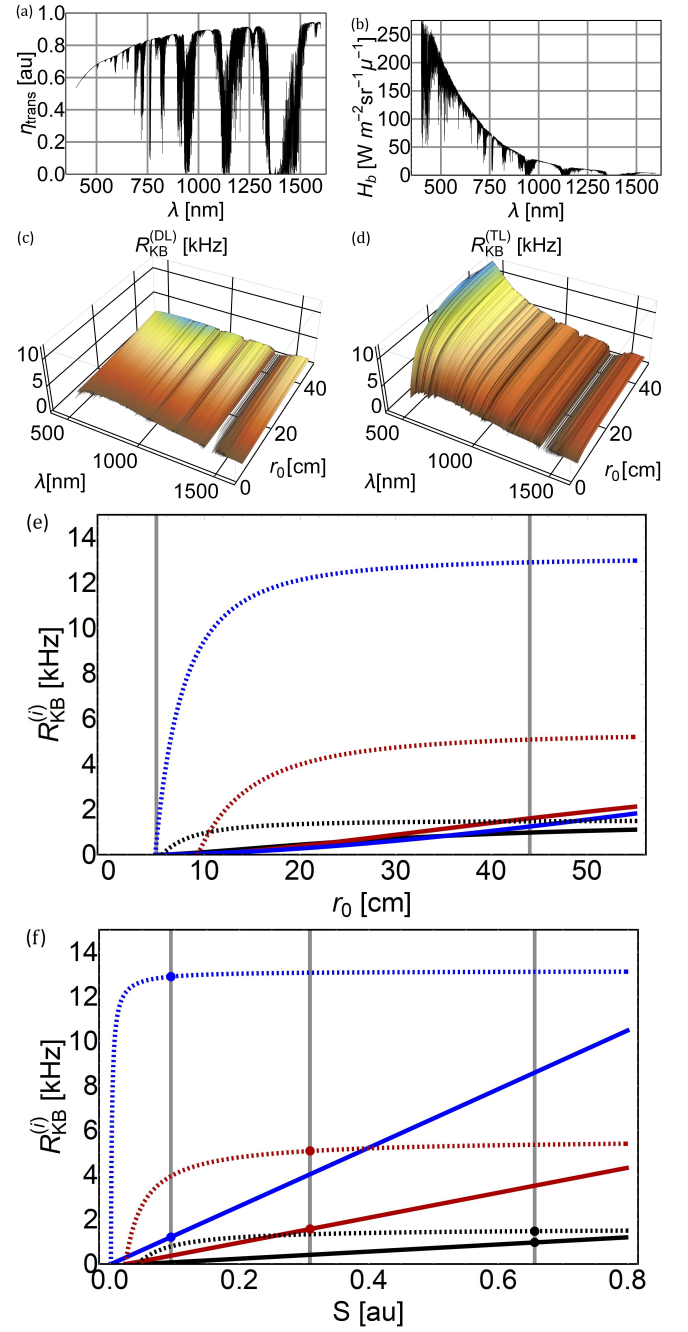


FIG. 14: The (a-b) atmospheric transmission η_{trans} and spectral radiance H_b , and (c-d) the secret key rate $R_{\text{KB}}^{(i)}$ for summer solstice with medium visibility (23-km), plotted as a function of r_0 at 500-nm. In this case we have narrowed the spectral filter to $\Delta\lambda = 0.05$ -nm. In (e-f) we have chosen 1550-, 781-, and 405-nm (black, red, and blue respectively), and the solid and dashed curves indicate the DL and TL strategies, respectively.

In (e) the vertical lines at $r_0^{(\text{OL})} = 5$ -cm and $r_0^{(\text{CL})} = 44$ -cm indicate the effective r_0 corresponding to an example of open- and closed-loop AO operation, respectively. In (f) the λ dependence of S produces three vertical lines indicating AO correction.

key bit yield even at $r_0 \approx 5$ -cm with both 1550- and 405-nm for the high-visibility condition. In Fig. 13(f) and 14(f) we plot we plot $R_{\text{KB}}^{(i)}$ as a function of system Strehl. Tighter spectral filtering reveals the trend in Strehl even more clearly, that is, short wavelengths with the TL strategy permit very high performance even with relatively low Strehl. Therefore, our simulation demonstrates how one can choose an optimal wavelength and filtering strategy for even the most challenging down-link conditions.

IV. CONCLUSION

In this article we investigate the ideal wavelength for free-space quantum communication over space-Earth quantum channels, particularly in daytime conditions where filtering sky-noise photons is a formidable challenge. Ultimately, the performance of a free-space quantum-communication system depends on the amount of signal and noise passing through the optical receiver spatial filter. However, the performance is an effect of quantum phenomenon and a simple analysis can be quite misleading. Therefore, we integrate the physics of focusing in the presence of atmospheric turbulence with the decoy-state BB84-QKD protocol, thus establishing an actual quantum-performance metric. We carefully examine the wavelength and spatial coherence r_0 (Fried coherence length) dependence of each component of the protocol. Namely, we investigate the dependence of the optical receiver field of view, the resulting number of sky-noise photons, the quantum bit error rate, and the signal-to-noise ratio.

Ultimately, we derive the QKD bit yield as a function of wavelength and spatial coherence r_0 , and investigate two different spatial-filtering strategies. Although the quantum bit error rate and signal-to-noise ratio do not considerably change with the two strategies, one strategy has a clear advantage due to the boost in signal. We show that, in general, shorter wavelengths outperform longer wavelengths for a wide range of channel conditions. There is a relatively large dip in spectral radiance H_b near 431-nm that permits the highest QKD-system performance over the entire visible spectrum and into

the telecom band when using a 1-nm spectral filter. This persists for several channel conditions representative of a space-Earth down-link architecture, namely winter and summer solstices with visibilities ranging from 50- to 5-km. We show how aggressive spectral filtering can permit high performance under challenging channel conditions, but a trade study is necessary in the case of clipping by the spectral filter.

We also cast the optimization problem in terms of higher-order adaptive optics, which allows one to correct for atmospheric turbulence, in effect operating their optical receiver closer to the diffraction limit. This allows one to use very tight spatial filtering and relax other filtering requirements if need be, for example, for an entanglement based protocol with broader-band photons. Adaptive optics systems for shorter wavelengths are in general more difficult to construct due to, for example, the requirement of more wavefront sensor sub-apertures due to the wavelength dependence of $r(\lambda)$. However, our results show that even a relatively low performance AO system, for example an AO corrected Strehl of ~ 0.5 at a short wavelength, can provide significant performance benefit relative to longer wavelengths operating near the diffraction limit. We contend that in the context of the global-scale quantum internet mediated by free-space links, these engineering concerns pose relatively straightforward problems and warrant further investigation and investment.

For space based networks where there are no atmospheric effects, the optical receivers would naturally operate near the diffraction limit, and shorter wavelengths have the clear advantage due to the optimal geometric coupling. To complete a system design of a global-scale quantum network, an angle dependent study including the effects of scintillation might be required for cases with large Zenith angles. Furthermore, a careful analysis including the spectral radiance due to Earth shine and turbulence induced beam spreading should also be considered for the up-link scenario.

ACKNOWLEDGMENTS

This work was supported by the Office of the Secretary of Defense (OSD) ARAP Defense Optical Channel Program (DOC-P).

-
- [1] H. T. Friis, IEEE spectrum **8**, 55 (1971).
 - [2] S. B. Alexander, *Optical communication receiver design*, 37 (IET, 1997).
 - [3] R. Van Meter, *Quantum networking* (John Wiley & Sons, 2014).
 - [4] K. Boone, J.-P. Bourgoin, E. Meyer-Scott, K. Heshami, T. Jennewein, and C. Simon, Physical Review A **91**, 052325 (2015).
 - [5] S. Wehner, D. Elkouss, and R. Hanson, Science **362** (2018).
 - [6] W. T. Buttler, R. J. Hughes, S. K. Lamoreaux, G. L. Morgan, J. E. Nordholt, and C. G. Peterson, Physical Review Letters **84**, 5652 (2000).
 - [7] R. J. Hughes, J. E. Nordholt, D. Derkacs, and C. G. Peterson, New journal of physics **4**, 43 (2002).
 - [8] X. Shan, X. Sun, J. Luo, Z. Tan, and M. Zhan, Applied physics letters **89**, 191121 (2006).
 - [9] M. P. Peloso, I. Gerhardt, C. Ho, A. Lamas-Linares, and C. Kurtsiefer, New Journal of Physics **11**, 045007 (2009).
 - [10] B. Heim, D. Elser, T. Bartley, M. Sabuncu, C. Wittmann,

- D. Sych, C. Marquardt, and G. Leuchs, *Applied Physics B* **98**, 635 (2010).
- [11] M. García-Martínez, N. Denisenko, D. Soto, D. Arroyo, A. Orue, and V. Fernandez, *Applied optics* **52**, 3311 (2013).
- [12] A. Carrasco-Casado, N. Denisenko, and V. Fernandez, *Optical Engineering* **53**, 084112 (2014).
- [13] M. T. Gruneisen, M. B. Flanagan, B. A. Sickmiller, J. P. Black, K. E. Stoltenberg, and A. W. Duchane, *Optics Express* **23**, 23924 (2015).
- [14] M. T. Gruneisen, B. A. Sickmiller, M. B. Flanagan, J. P. Black, K. E. Stoltenberg, and A. W. Duchane, *Optical Engineering* **55**, 026104 (2016).
- [15] M. T. Gruneisen, M. B. Flanagan, and B. A. Sickmiller, *Optical Engineering* **56**, 126111 (2017).
- [16] S.-K. Liao, H.-L. Yong, C. Liu, G.-L. Shentu, D.-D. Li, J. Lin, H. Dai, S.-Q. Zhao, B. Li, J.-Y. Guan, et al., *Nature Photonics* **11**, 509 (2017).
- [17] D. Vasylyev, A. Semenov, W. Vogel, K. Günthner, A. Thurn, Ö. Bayraktar, and C. Marquardt, *Physical Review A* **96**, 043856 (2017).
- [18] P. Arteaga-Díaz, A. Ocampos-Guillén, and V. Fernandez, in *2019 21st International Conference on Transparent Optical Networks (ICTON)* (IEEE, 2019), pp. 1–4.
- [19] M. T. Gruneisen, M. L. Eickhoff, S. C. Newey, K. E. Stoltenberg, J. F. Morris, M. Bareian, M. A. Harris, D. W. Oesch, M. D. Oliker, M. B. Flanagan, et al., arXiv preprint arXiv:2006.07745 (2020).
- [20] J. E. Nordholt, R. J. Hughes, G. L. Morgan, C. G. Peterson, and C. C. Wipf, in *Free-Space Laser Communication Technologies XIV* (International Society for Optics and Photonics, 2002), vol. 4635, pp. 116–126.
- [21] J. Bourgoïn, E. Meyer-Scott, B. L. Higgins, B. Helou, C. Erven, H. Huebel, B. Kumar, D. Hudson, I. D’Souza, R. Girard, et al., *New J. Phys* **15**, 023006 (2013).
- [22] C. H. Bennett and G. Brassard, arXiv preprint arXiv:2003.06557 (2020).
- [23] X. Ma, B. Qi, Y. Zhao, and H.-K. Lo, *Physical Review A* **72**, 012326 (2005).
- [24] D. L. Fried, *JOSA* **56**, 1372 (1966).
- [25] J. H. Shapiro, *Physical Review A* **84**, 032340 (2011).
- [26] T. C. Farrell, *Sensors and Systems for Space Applications* **11017** (2019).
- [27] M. C. Roggemann, B. M. Welsh, and B. R. Hunt, *Imaging through turbulence* (CRC press, 1996).
- [28] L. C. Andrews, *Field guide to atmospheric optics* (SPIE Press,, 2004).
- [29] A. Tomaello, A. Dall’Arche, G. Naletto, and P. Villorresi, in *Quantum Communications and Quantum Imaging IX* (International Society for Optics and Photonics, 2011), vol. 8163, p. 816309.
- [30] C. Bonato, A. Tomaello, V. Da Deppo, G. Naletto, and P. Villorresi, *NJP* **11**, 045017 (2009).
- [31] R. K. Tyson, *Principles of adaptive optics* (CRC press, 2015).

Appendix A: Wavelength dependence of AO correction

1. Residual Error

In a higher-order AO system, the aberrations of the incoming wavefront are corrected via a deformable mirror (DM) imprinted with the conjugate of the wavefront error. The system is run in a closed-loop configuration in which a small portion of the light output from the DM is split off into a wavefront sensor which measures the residual phase error (RPE) of the wavefront, and is used to update the DM. This makes the RPE perhaps the most fundamental parameter related to AO system performance. For the open-loop case, the RPE variance in radians σ_ϕ^2 depends primarily on the spatial coherence at the receiver aperture and one can write [28]

$$\sigma_{\phi,OL}^2 = 1.03 \left(\frac{D_R}{r(\lambda)} \right)^{5/3}, \quad (\text{A1})$$

where the OL subscript indicates open-loop operation and $r(\lambda)$ can be calculated according to [28]

$$r(\lambda) = \left[0.423 k^2 \sec(\theta_z) \int_0^a dh C_n^2(h) \right]^{-3/5}, \quad (\text{A2})$$

where $C_n^2(h)$ is the atmospheric turbulence structure parameter, θ_z is the zenith angle, a is the altitude of the light source, and $k = 2\pi/\lambda$. One should note that the wavelength dependence of Eq. A2 is the origin of the wavelength dependence of Eq. 5, that is, $(k^2)^{-3/5} \propto (\lambda^{-2})^{-3/5} = \lambda^{6/5}$. Furthermore, as specified in the main text, we assume r_0 is the value calculated at 500-nm and therefore $r_0 \equiv r(500\text{-nm})$ using Eq. A2.

For a closed-loop AO system the RPE is dominated by the systems ability to keep pace with the temporal component of the atmospheric fluctuations characterized by the Greenwood frequency [28]

$$f_G = \left[0.1022 k^2 \sec(\theta_z) \int_0^a dh C_n^2(h) v_w^{5/3}(h) \right]^{3/5}, \quad (\text{A3})$$

where $v_w(h)$ is the wind model. The closed-loop RPE can be written in terms of the closed-loop bandwidth of the AO system f_c according to [31]

$$\sigma_{\phi,CL}^2 = \left(\frac{f_G}{f_c} \right)^{5/3}. \quad (\text{A4})$$

This expression is independent of r_0 as long as ones wavefront sensor is judiciously designed such that the wavefront error is efficiently spatially resolved. One might assume that the AO system needs to respond faster than the Greenwood frequency in order to provide adequate compensation. However, we have shown through numerical simulations that an AO system can substantially enhance the performance of a QKD system even if it is several times slower than the Greenwood frequency. [15]

Both Eq. A1 and Eq. A4 can be used to find the Optical-Path-Difference (OPD) variance

$$\sigma_{\text{nm}}^2 = \sigma_{\phi}^2 \left(\frac{\lambda}{2\pi} \right)^2. \quad (\text{A5})$$

The OPD variance in nanometers is a useful quantity because it is independent of wavelength. Using Eqs. A1, A5, and 5 one can show that

$$\sigma_{\text{nm,OL}}^2 = 1.03 \left(\frac{500}{2\pi} \right)^2 \left(\frac{D_{\text{R}}}{r_0} \right)^{5/3}, \quad (\text{A6})$$

where r_0 is the Fried coherence length measured at 500-nm. Therefore, the open-loop OPD variance $\sigma_{\text{nm,OL}}^2$ is a property of the atmosphere that is directly measured by the wavefront sensor when the AO system is in the open-loop configuration, that is, a flat DM. For the closed-loop case, we combine Eqs. A3, A4, and A5 to find

$$\sigma_{\text{nm,CL}}^2 = \left(\frac{1}{2\pi} \right)^2 \left(\frac{2.31}{f_c} \right)^{5/3} \times \sec(\theta_z) \int_0^a dh C_n^2(h) v_w^{5/3}(h). \quad (\text{A7})$$

Therefore, one can see that the closed-loop OPD variance $\sigma_{\text{nm,CL}}^2$ depends on the relationship between the closed-loop bandwidth and the temporal component of the turbulence characterized by the integral.

2. Effective Fried Coherence and Closed-Loop Bandwidth

We wish to interpret the r_0 dependence of R_{KB} and each of the contributing phenomenon in terms of AO. To do so, we would like to establish an effective r_0 corresponding to residual turbulence effects after AO correction. Hence, we will assume for the moment that the RPE variance for open- and closed-loop operation are equal. This permits one to equate Eqs. A1 and A4 and solve for r_0 :

$$r_0^{(\text{CL})} = 1.03^{3/5} \left(\frac{500}{\lambda} \right)^{6/5} \frac{D_{\text{R}} f_c}{f_{\text{G}}}, \quad (\text{A8})$$

where the superscript CL indicates that this r_0 is the effective spatial coherence during closed-loop operation. In other words, with AO, a given combination of f_{G} and f_c yields the same optical receiver performance that would be achieved without AO in an atmosphere described by $r_0^{(\text{CL})}$. Similarly, one can solve for f_c and find

$$f_c^{(\text{OL})} = 1.03^{-3/5} \left(\frac{500}{\lambda} \right)^{-6/5} \frac{r_0 f_{\text{G}}}{D_{\text{R}}}, \quad (\text{A9})$$

where in this case the superscript OL indicates that this f_c is the effective closed-loop bandwidth of open-loop operation. In other words, $f_c^{(\text{OL})}$ is the closed-loop bandwidth that yields no improvement over open-loop optical

receiver performance. It also serves as the lower bound when investigating the f_c dependence of Eq. A4. Depending on the functional dependence of ones performance parameter, both of these equations can be used to show the relative improvement higher-order AO can provide. In the main text we do this by including vertical lines indicating the effective r_0 of higher-order AO correction and by plotting the key rate as a function of f_c in Fig. 10. In our article reporting our field experiment we use Eq. A8 to emphasize the level of correction possible with different bandwidth AO systems [19].

In Ref. [19] we carefully show how one can calculate the Fried coherence and slew dependent Greenwood frequency for a circular orbit passing overhead. The emphasis therein was to indicate the equivalent horizontal-path propagation length corresponding to slant-path propagation. Since we have limited our study to zenith, we set $\theta_z = 0$ and using the slant-path expressions we find $r_0 \approx 5$ -cm and $f_{\text{G}}(500\text{-nm}) \approx 300$ -Hz. In our field experiment we built a $f_c = 130$ -Hz AO system for compensation of temporal characteristics corresponding to a 1.6-km horizontal channel where the maximum observed f_{G} was approximately 60-Hz. For the down-link scenario, one would in practice build a much faster AO system that can more effectively compensate for the temporal component of the turbulence. However, for this simulation we assume $f_c = 130$ -Hz in order to demonstrate there is not a sharp cutoff in effectiveness and even a relatively slow system, that is, a system slower than the observed Greenwood frequency, can still provide a substantial boost in QKD performance if the proper spatial filtering strategy is adopted. Therefore, using $f_{\text{G}} = 300$ - and $f_c = 130$ -Hz in Eq. A8 we find $r_0^{(\text{CL})} \approx 44$ -cm and use this throughout the main text to indicate an example of closed-loop AO operation. Examining Eq. A8 one will notice the linear relationship between r_0 and f_c . Therefore, one can easily envision how increasing AO system bandwidth scales up the QKD system performance.

3. Strehl

Another performance parameter closely related to AO systems is the system Strehl. Using Eq. A1 and A5 in Eq. 4, one can rewrite the Strehl as

$$S = \left[1 + \frac{1}{1.03} \sigma_{\text{nm}}^2 \left(\frac{2\pi}{\lambda} \right)^2 \right]^{-6/5}. \quad (\text{A10})$$

This is significant because it shows that a AO system has a wavelength-dependent system Strehl. Using Eq. A5 we find $\sigma_{\text{nm,OL}}^2 \approx 980$ -nm and using Eq. A5 in conjunction with Eq. A8 we find $\sigma_{\text{nm,CL}}^2 \approx 160$ -nm. In Fig. 15 we plot the system Strehl for 1550-, 781-, and 431-nm (black, red, and blue respectively) as a function of σ_{nm} . The vertical line on the left (right) indicates the σ_{nm} corresponding to closed-loop (open-loop) operation. The horizontal lines indicate the achieved closed-loop Strehl at each wavelength. Therefore, one can see that a short-wavelength

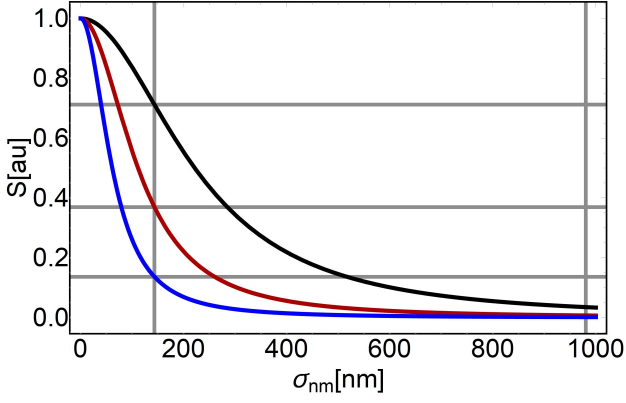


FIG. 15: The system Strehl for 1550-, 781-, and 431-nm (black, red, and blue respectively), plotted as a function of σ_{nm} . The vertical lines indicate the σ_{nm} of a closed- and open-loop AO system correcting for an atmosphere characterized by $r_0 = 5$ -cm. The horizontal lines indicate the achieved closed-loop Strehl at each wavelength.

closed-loop AO system will operate at a much lower system Strehl. In the main text we investigate how this affects the performance of the QKD system.

4. Spot Size

The wavelength dependence of the sky background H_b and the geometric coupling are important components of the optimization problem, but the most fundamental physics pertains to the focused spot size and its dependence on wavelength. Equation 5 shows that longer wavelengths are affected less by a given atmospheric condition, but Eq. 1 shows that, in the absence of turbulence, the focused spot is larger, resulting in either more loss at the spatial filter or more noise, depending on the spatial filter strategy. On the other hand, the shorter wavelength has a smaller focused spot but is impacted more by the atmosphere. We will now investigate these competing trends in terms of the residual error. Using Eq. A10 in Eq. 3 one can write

$$d_{\text{spot}}^{(\text{TL})} = d_{\text{spot}}^{(\text{DL})} \left[1 + \frac{1}{1.03} \sigma_{\text{nm}}^2 \left(\frac{2\pi}{\lambda} \right)^2 \right]^{3/5}, \quad (\text{A11})$$

which can be used to find the TL FOV

$$\Omega_{\text{FOV}}^{(\text{TL})} = \pi \left(1.22 \frac{\lambda}{D_R} \left[1 + \frac{1}{1.03} \sigma_{\text{nm}}^2 \left(\frac{2\pi}{\lambda} \right)^2 \right]^{3/5} \right)^2. \quad (\text{A12})$$

In Fig. 16 we use Eq. A12 to plot the linear-angle FOV as a function of OPD standard deviation σ_{nm} (this figure is an analog to Fig. 3 which was a function of r_0). This open-loop scenario can be seen in Fig. 16(b) where one will notice that the strong wavelength dependent atmospheric effects are dominant here and the FOV's are

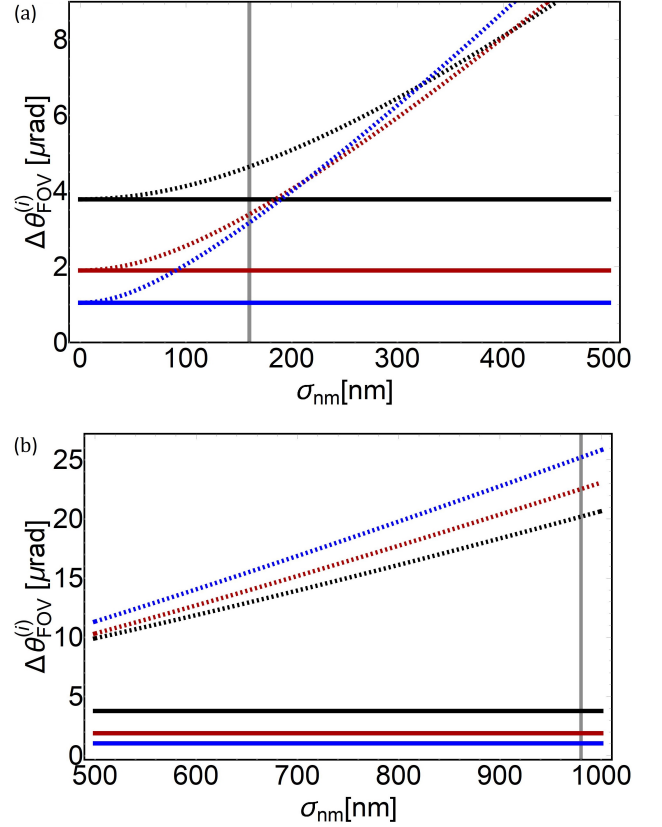


FIG. 16: The linear angle FOV for 1550-, 781-, and 431-nm (black, red, and blue respectively), plotted as a function of σ_{nm} for (a) 0- to 500-nm and (b) 500- to 1000-nm. The solid and dashed curves indicate the DL and TL FOV's, respectively. The vertical lines indicate the σ_{nm} of a closed-loop ($\sigma_{\text{nm}} \approx 160$ -nm) and open-loop ($\sigma_{\text{nm}} \approx 980$ -nm) AO system correcting for an atmosphere characterized by $r_0 = 5$ -cm.

larger for the short wavelengths. In Fig. 16(a) we plot the range for a well-functioning AO system. One will see that in the 300- to 400-nm range there is a transition where the wavelength dependence of spot size begins to dominate and shorter wavelengths permit a smaller FOV's.

Appendix B: Optimal Wavelength for Decoy-State BB84-QKD

We chose wavelengths near 1550- and 780-nm because these are common wavelengths considered for space-Earth quantum communications. To find a true optimal wavelength we investigate the wavelength dependence of the key rate $R_{\text{SKB}}^{(\text{TL})}$ for winter solstice with high visibility over a large wavelength range. In Figs. 17(a) and 17(b) we plot the key rate for two different wavelength ranges. We assume $f_c = 130$ -Hz AO system yielding $r_0^{(\text{CL})} = 44$ -cm is utilized. Furthermore, the black and

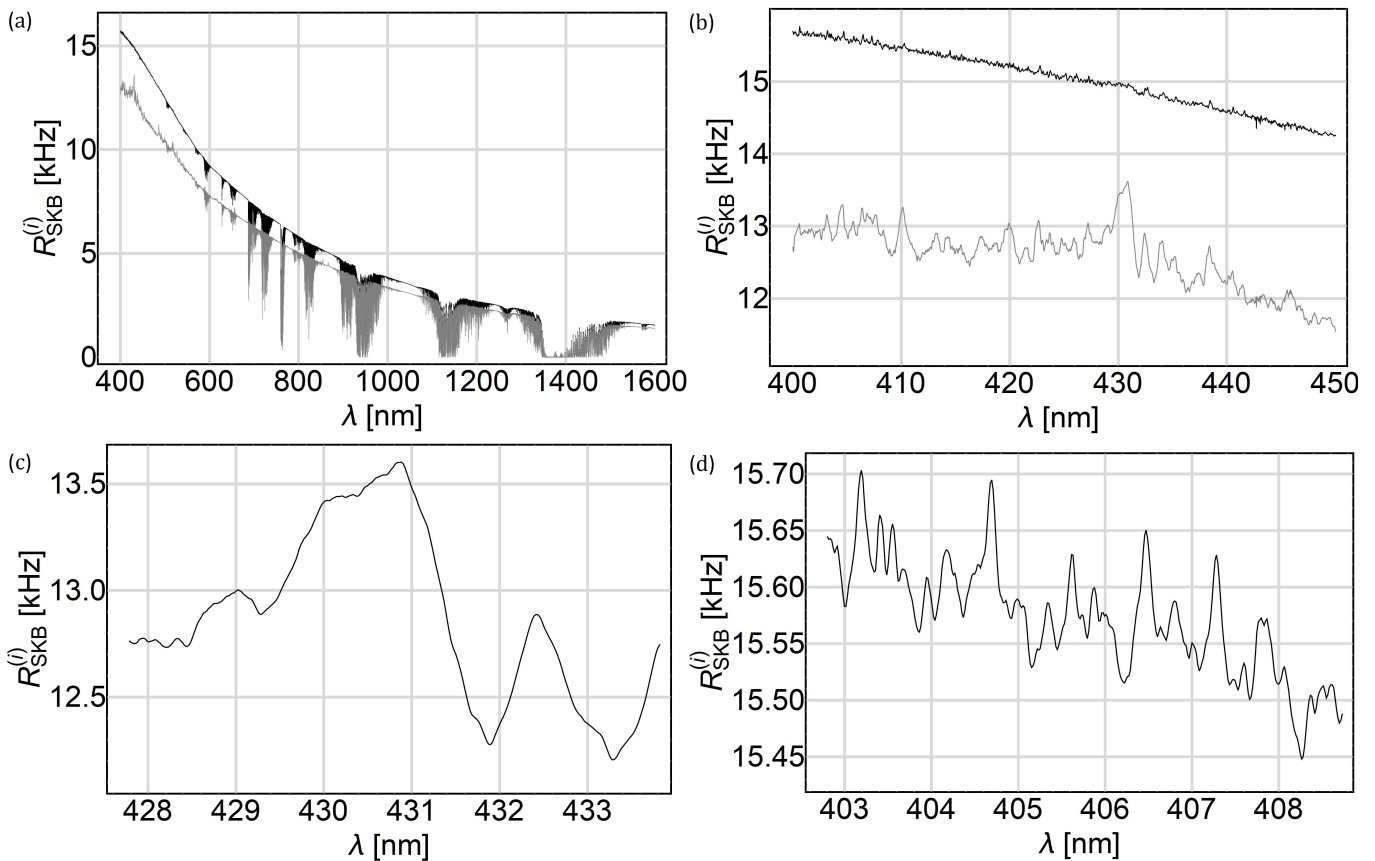


FIG. 17: The key rate $R_{\text{KB}}^{(\text{TL})}$ for winter solstice with high visibility and $r_0 = 44$ -cm. In (a) and (b) we give the key rate for a 1-nm (0.05-nm) filter in gray (black). In (c) and (d) we zoom in to reveal a range of optimal wavelengths for a 1-nm and 0.05-nm filter, respectively.

gray curves represent the key rate for 0.05-nm and 1-nm spectral filters, respectively. One can see that although the sky is generally brighter and transmission is poorer at shorter wavelengths, the key key rates are generally higher. In Figs. 17(b-d) we zoom in to the shorter wavelength range and reveal the optimal wavelength for the

site condition using the two different filters. For the 1-nm filter we find the optimal wavelength $\lambda_{\text{opt}}^{(1\text{-nm})} = 430.886$ -nm and for the 0.05-nm filter there is a convenient peak at $\lambda_{\text{opt}}^{(0.05\text{-nm})} = 404.694$ -nm (see Figs. 17(c) and 17(d), respectively). These features persist for the more challenging visibility conditions and we therefore use these wavelengths throughout the investigation.